nature medicine

Multiparametric optical analysis of mitochondrial redox signals during neuronal physiology and pathology *in vivo*

Michael O Breckwoldt[1,2,11], Franz M J Pfister[1,2], Peter M Bradley[2], Petar Marinković[1], Philip R Williams[1], Monika S Brill[1], Barbara Plomer[1], Anja Schmalz[2], Daret K St Clair[3], Ronald Naumann[4], Oliver Griesbeck[5], Markus Schwarzländer[6], Leanne Godinho[1], Florence M Bareyre[2,7], Tobias P Dick[8], Martin Kerschensteiner[2,7,12] & Thomas Misgeld[1,7,9,10,12]

Mitochondrial redox signals have a central role in neuronal physiology and disease. Here we describe a new optical approach to measure fast redox signals with single-organelle resolution in living mice that express genetically encoded redox biosensors in their neuronal mitochondria. Moreover, we demonstrate how parallel measurements with several biosensors can integrate these redox signals into a comprehensive characterization of mitochondrial function. This approach revealed that axonal mitochondria undergo spontaneous 'contractions' that are accompanied by reversible redox changes. These contractions are amplified by neuronal activity and acute or chronic neuronal insults. Multiparametric imaging reveals that contractions constitute respiratory chain–dependent episodes of depolarization coinciding with matrix alkalinization, followed by uncoupling. In contrast, permanent mitochondrial damage after spinal cord injury depends on calcium influx and mitochondrial permeability transition. Thus, our approach allows us to identify heterogeneity among physiological and pathological redox signals, correlate such signals to functional and structural organelle dynamics and dissect the underlying mechanisms.

Reactive oxygen species (ROS) are key signaling molecules that regulate cell metabolism, migration, survival and regeneration[1–4]. However, excessive ROS levels can also lead to pathological oxidation of proteins, lipids and DNA. Such oxidative stress has emerged as a key mechanism of cellular damage during aging and disease[5,6]. ROS can be generated as a byproduct of mitochondrial oxidative phosphorylation in many cell types[1,7]. At the same time, mitochondria are primary targets of ROS-mediated damage, which can further accelerate their own ROS production[8]. Given the essential roles of mitochondria in bioenergetics, calcium buffering and apoptosis[9], such a 'vicious cycle' of ROS-mediated mitochondrial damage can have devastating consequences for the entire cell. Neurons, with their high energy demands and complex morphology, seem particularly vulnerable to such damage. Indeed, ROS-mediated mitochondrial damage has been implicated in acute neuronal injury, for example, after traumatic or inflammatory lesions[10–12], but also in chronic neurodegenerative conditions, including amyotrophic lateral sclerosis (ALS), Alzheimer's disease and Parkinson's disease[6].

The central challenge in analyzing the role of mitochondrial redox signals is their multifaceted nature, for which timing, location and concentration are critical. To better understand how redox signals exert their effects on neurons, we established a new *in vivo* imaging 'tool kit' to follow redox changes in neuronal mitochondria of mice with high temporal and spatial resolution. Our approach is based on (i) transgenic expression of glutaredoxin-1 (Grx1)–reduction-oxidation sensitive GFP2 (roGFP2), a biosensor for the glutathione redox potential[2,13], in neuronal mitochondria, (ii) excitation-ratiometric wide-field, confocal and two-photon measurement of the biosensor's redox state with subcellular resolution in a range of axon populations[14] and in mouse models of ALS[15] and spinal cord injury[16] and (iii) parallel measurements of mitochondrial membrane potential and pH, as well as of mitochondrial and axonal calcium levels[17], which integrate redox signals into a comprehensive view of mitochondrial function.

This multiparametric *in vivo* imaging approach allowed us to reveal fast physiological and pathological redox signals in single mitochondria and dissect their molecular causes and morphological consequences. Under physiological conditions, the mitochondrial glutathione redox potential in neurons was tightly regulated and independent of organelle location or movement. Notably, however, individual mitochondria showed spontaneous and reversible contractions that were accompanied by short-lived oxidative bursts. These spontaneous events were present under physiological conditions and increased in frequency if the neuron was stressed, for example,

[1]Institute for Neuronal Cell Biology, Technical University Munich, Munich, Germany. [2]Institute of Clinical Neuroimmunology, Ludwig-Maximilians University Munich, Munich, Germany. [3]Graduate Center for Toxicology and Markey Cancer Center, University of Kentucky College of Medicine, Lexington, Kentucky, USA. [4]Transgenic Core Facility, Max Planck Institute of Molecular Cell Biology and Genetics, Dresden, Germany. [5]Max-Planck Institute of Neurobiology, Martinsried, Germany. [6]Institute of Crop Science and Resource Conservation (INRES), University of Bonn, Bonn, Germany. [7]Munich Cluster for Systems Neurology (SyNergy), Munich, Germany. [8]Division of Redox Regulation, German Cancer Research Center (DKFZ), Heidelberg, Germany. [9]German Center for Neurodegenerative Diseases (DZNE), Munich, Germany. [10]Center for Integrated Protein Sciences (CIPS), Munich, Germany. [11]Present address: Department of Neuroradiology, University of Heidelberg, Heidelberg, Germany. [12]These authors contributed equally to this work. Correspondence should be addressed to M.K. (martin.kerschensteiner@med.uni-muenchen.de) or T.M. (thomas.misgeld@lrz.tu-muenchen.de).

Received 1 July 2013; accepted 4 September 2013; published online 20 April 2014; doi:10.1038/nm.3520

by electrical stimulation, nerve crush or chronic neurodegeneration. Contractions depended on respiratory chain activity and were characterized by reversible changes to the mitochondrial membrane potential, pH and glutathione redox state. Such transient mitochondrial stress responses contrasted with longer-lasting mitochondrial shape and redox changes that were induced by more severe injuries, such as axotomy. *In vivo* two-photon and confocal imaging after spinal cord injury revealed that axotomy-induced mitochondrial oxidation and damage were initiated at the transection site and subsequently spread along the axon. Notably, these spreading mitochondrial changes were preceded by a calcium rise that traveled along the axon with about twice the speed of the redox change and that induced an abrupt increase in mitochondrial calcium. *In vivo* pharmacological and genetic interventions showed that calcium influx initiated the spread of mitochondrial oxidation and subsequent organelle pathology. In contrast to reversible contractions, these axotomy-induced permanent alterations were accompanied by transition pore opening and could not be prevented by ROS scavenging. Thus our new 'optobioenergetic' approach allowed us to discover previously uncharacterized mitochondrial redox signals in health and disease and to dissect *in vivo* the relationships between such signals, the accompanying organelle dynamics and the underlying mechanisms.

RESULTS

In situ quantification of the mitochondrial redox state

We developed an *in vivo* imaging approach to measure mitochondrial redox changes based on a recently generated redox biosensor in which Grx1 is fused to the redox-sensitive fluorescent protein roGFP2 (refs. 2,13). In principle, this sensor should be well suited for *in vivo* imaging, as it is a genetically encoded ratiometric indicator (in contrast to many redox-sensitive dyes)[18] that is not susceptible to pH changes in the physiological range (in contrast to circularly permuted YFP (cpYFP)-based sensors, such as HyPer)[19,20] and allows imaging of fast dynamics (in contrast to conventional roGFP)[21,22]. To evaluate this sensor for *in vivo* use in neuronal mitochondria, we generated *Thy1*-mito-Grx1-roGFP2 mice, in which biosensor expression was restricted to neuronal mitochondria by combining a neuron-specific version of the *Thy1* promoter and a mitochondrial targeting sequence. We obtained 11 founder lines and characterized their expression pattern in the peripheral and central nervous systems (**Fig. 1a–c**). Several *Thy1*-mito-Grx1-roGFP2 lines displayed brightly labeled peripheral and central neurons (**Supplementary Table 1**). These mice were viable, fertile and showed no neurological abnormalities (**Supplementary Fig. 1**).

Using a polychromator-equipped wide-field microscope to rapidly alternate the excitation wavelength between 408 and 488 nm, we calibrated the sensor in triangularis sterni nerve-muscle explants of *Thy1*-mito-Grx1-roGFP2 mice after exogenous application of hydrogen peroxide (H_2O_2) (**Fig. 1d,e**). The dose-response curve spanned a broad concentration range of applied H_2O_2 (6.25–800 µM), in accordance with the *in vitro* characteristics of this sensor[13]. After application of a reducing agent, dithiothreitol (DTT), the 408/488 nm ratio dropped below the levels measured in oxygenated Ringer's solution (without H_2O_2), indicating partial oxidation of the sensor under baseline conditions. This suggested that physiological redox signals should be detectable in this setting. Indeed, whereas we observed a stable and comparable redox state in most resting and moving axonal mitochondria (**Fig. 1f** and **Supplementary Video 1**), in some mitochondria, we detected spontaneous oxidative bursts (**Fig. 2a,b** and **Supplementary Video 2**). Notably, these bursts were accompanied by reversible shape changes, which we named mitochondrial contractions (contraction frequency per mitochondrion: 0.6 ± 0.1 per hour; n = 594 mitochondria observed in 14 recordings, three mice).

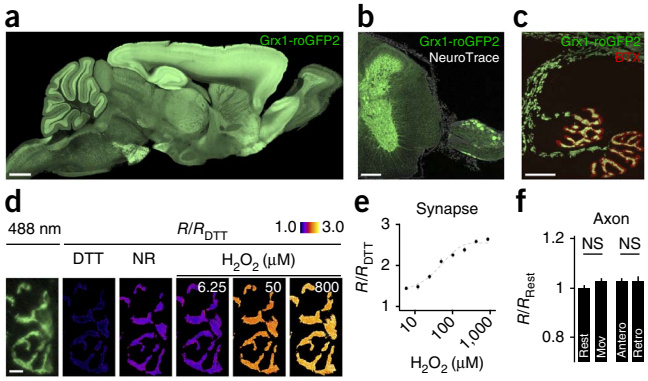

Figure 1 *Thy1*-mito-Grx1-roGFP2 mice allow quantification of the mitochondrial glutathione redox potential *in situ*. (**a–c**) Sensor expression pattern in the central and peripheral nervous systems of *Thy1*-mito-Grx1-roGFP2 mice. Representative images show a sagittal brain overview (**a**), a horizontal spinal cord section (**b**) and neuromuscular junctions (NMJs) (**c**) of *Thy1*-mito-Grx1-roGFP2 mice. BTX, α-bungarotoxin ($n \geq 5$ mice). (**d**) Representative wide-field image (left) and ratiometric pseudocolored images (right) of the same NMJ during the addition of 500 µM of the reducing agent DTT, of normal Ringer's solution (NR) or of the oxidant H_2O_2 in concentrations shown. (**e**) Dose-response curve of the sensor measured at NMJs shows a dynamic range of 2.6 (n = 15–35 synapses per concentration from 4 mice). (**f**) Glutathione redox potential in different (Rest, resting; Mov, moving; Antero, anterograde; Retro, retrograde) populations of axonal mitochondria (normalized to resting mitochondria; n = 44–132 mitochondria per group from 3 mice). NS, not significant. R/R_{DTT}, fluorescence ratio normalized to ratio after reduction with DTT. Graphs show mean ± s.e.m. Scale bars, 1 mm in **a**, 200 µm in **b**, 20 µm in **c** and 5 µm in **d**.

Multiparametric imaging of mitochondrial contractions

Although paroxysmal changes of mitochondrial function have been observed previously[23], the *in vivo* characteristics and mechanistic underpinnings of such phenomena are poorly understood. We therefore set out to dissect the mechanism underlying mitochondrial contractions by multiparametric imaging of mitochondrial function. We assayed the mitochondrial membrane potential by *in vivo* application of tetramethylrhodamine methyl ester perchlorate (TMRM) and measured mitochondrial pH and calcium levels by adeno-associated virus (AAV)-mediated gene transfer of mitochondrially targeted sensors of pH (rAAV-mito–synthetic pH sensor (SypHer)[24] or rAAV-mito-R-GECO1 (ref. 25)) in motor neurons. We found that the onset of contractions coincided with rapid mitochondrial depolarization as well as a sharp initial alkaline spike in the mitochondrial matrix that was followed by gradual matrix acidification (**Fig. 2c–f** and **Supplementary Video 3**). Both pH and membrane potential changes then slowly started to recover. In contrast to other paroxysmal changes in mitochondria[26], contractions were not accompanied by measurable changes in matrix calcium (**Fig. 2g,h**; signals measured with R-GECO1 during contractions were <1.5% of the dynamic range of the sensor as revealed, for example, by axotomy, as described below). To better understand the molecular mechanisms that underlie these changes, we combined functional imaging with *in situ* pharmacological and genetic manipulations. We found that inhibition of mitochondrial respiratory chain complex I by rotenone decreased the frequency of contractions in a dose-dependent manner (0.1 nM rotenone, 0.51 ± 0.22 of baseline contraction frequency, $P > 0.05$;

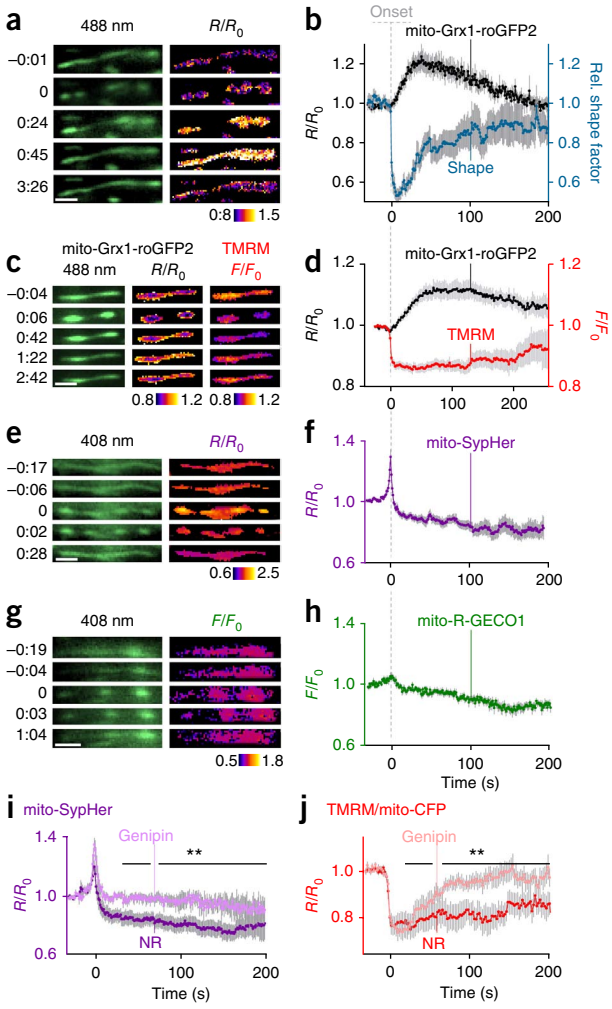

Figure 2 Mitochondria undergo spontaneous, reversible contractions. (**a**) Contracting mitochondrion in a triangularis sterni explant derived from a *Thy1*-mito-Grx1-roGFP2 mouse (time in minutes and seconds before and after contraction onset). (**b**) Graph showing the relationship between relative mitochondrial shape factor (Rel. shape factor) and probe oxidation during contractions ($n = 9$ contractions from 5 mice). (**c**) Contracting mitochondrion in a *Thy1*-mito-Grx1-roGFP2 explant loaded with the membrane potential–sensitive dye TMRM. (**d**) Quantification of the mitochondrial membrane potential and the glutathione redox potential during contractions ($n = 15$ contractions from 3 mice). (**e**) Contracting mitochondrion in a triangularis sterni explant derived from a wild-type mouse injected with rAAV-mito-SypHer. (**f**) Quantification of the mitochondrial pH during contractions ($n = 23$ contractions from 6 mice). (**g**) Contracting mitochondrion in a triangularis sterni explant derived from a wild-type mouse injected with rAAV-mito-R-GECO1 (408-nm channel signal derived from the co-injected rAAV-mito-SypHer is shown on the left). (**h**) Quantification of the mitochondrial matrix calcium during contractions ($n = 23$ contractions from 3 mice). (**i**) Quantification of the matrix pH in normal Ringer's solution and during genipin treatment (100 µM; $n = 12$–15 contractions from 3 mice per group; black line indicates the time period averaged for statistical analysis, $^{**}P < 0.01$, two-tailed *t*-test). (**j**) Quantification of the mitochondrial potential in normal Ringer's solution and during genipin treatment (100 µM) in explants of *Thy1*-mito-CFP mice loaded with TMRM ("TMRM/mito-CFP") ($n = 17$–29 contractions from 3 mice per group; black line indicates the time period averaged for statistical analysis, $^{**}P < 0.01$, two-tailed *t*-test). R/R_0, fluorescence ratio normalized to ratio at baseline; F/F_0, fluorescence intensity normalized to intensity at baseline. Graphs show mean ± s.e.m. Scale bars, 2 µm.

100 nM rotenone, 0.13 ± 0.05, $P < 0.001$; $n = 6$–11 recordings, two mice per group), indicating that contractions required active mitochondrial electron transport. Further, uncoupling proteins might contribute to the later stages of mitochondrial contractions, as an inhibitor of these proteins, genipin (100 µM), reduced the sustained acidification and accelerated the repolarization of mitochondria (**Fig. 2i,j**). In line with the absence of mitochondrial calcium signals, neither application of an inhibitor of the mitochondrial uniporter, Ru360 (100 µM, 1.7 ± 0.24 of baseline contraction frequency), nor suppressing mitochondrial permeability transition using cyclosporine (20 µM, 1.4 ± 0.3) or genetic deletion of cyclophilin D[27] (0.9 ± 0.1) significantly reduced contraction frequencies ($P > 0.05$, $n \geq 13$ recordings, three mice for all groups).

Next, we asked what might initiate contractions in individual mitochondria while leaving their neighbors unaffected. Measurements of the glutathione redox potential in single Grx1-roGFP2–labeled mitochondria revealed that contracting mitochondria showed a slight oxidative shift during the 30 s preceding the contraction, suggesting that pro-oxidative changes induced contractions (408/488 nm ratio: non-contracting 0.45 ± 0.01, $n = 279$, versus contracting 0.49 ± 0.01, $n = 32$, $P < 0.05$). Accordingly, exogenous application of H_2O_2 increased contraction frequency, whereas presence of the reducing agent DTT or the mitochondrial antioxidant MitoQ, as well as transgenic overexpression of mitochondrial manganese superoxide dismutase (MnSOD)[28], reduced their frequency (**Fig. 3a**). Thus, mitochondrial contractions might represent a stress-induced reaction of mitochondria. We tested this by exposing axons to physiological stressors, such as increased neuronal activity, or pathological stressors, including nerve crush and chronic neurodegeneration in an ALS model ($SOD1^{G93A}$ mice)[15], all of which increased mitochondrial oxidation and contraction frequency (**Fig. 3b–e** and **Supplementary Fig. 2**). Further, under these pathological conditions, the length of contractions was increased compared to baseline (**Fig. 3f** and **Supplementary Fig. 2**). This suggests that at noxious levels of stress, more permanent mitochondrial transitions might occur. Indeed, in ALS model mice with prolonged disease, axonal mitochondria were irreversibly rounded and oxidized (**Supplementary Fig. 2**).

In vivo analysis of injury-induced mitochondrial changes

To explore whether our *in vivo* approach to redox signaling would also allow a mechanistic characterization of longer-lasting mitochondrial changes induced by nervous system pathology, we turned to models of trauma. To optimize resolution of our method for post-traumatic changes, we first performed laser microsurgery[29] in the triangularis sterni explants, which yielded spatially and temporally well-controlled transections of large-caliber axons. Axotomy-induced mitochondrial rounding or fragmentation started immediately after transection (<5 s) at the axotomy site and then spread along the axon over the next few minutes (**Supplementary Fig. 3** and **Supplementary Video 4**). Multiparametric imaging, as outlined above, then revealed that these irreversible changes were accompanied by high-level mitochondrial oxidation and acidification, as well as an increase in matrix calcium (**Supplementary Fig. 3** and **Supplementary Video 5**).

To investigate whether similar mitochondrial alterations can also be observed after injury of the spinal cord, we developed a multiphoton-based redox imaging approach to visualize mitochondria in central nervous system axons *in vivo*. We first determined the two-photon excitation spectrum of the oxidized and reduced Grx1-roGFP2 sensor in the spinal cord of *Thy1*-mito-Grx1-roGFP2 mice (**Supplementary Fig. 4**). Based on these experiments, we excited sequentially at 800 and

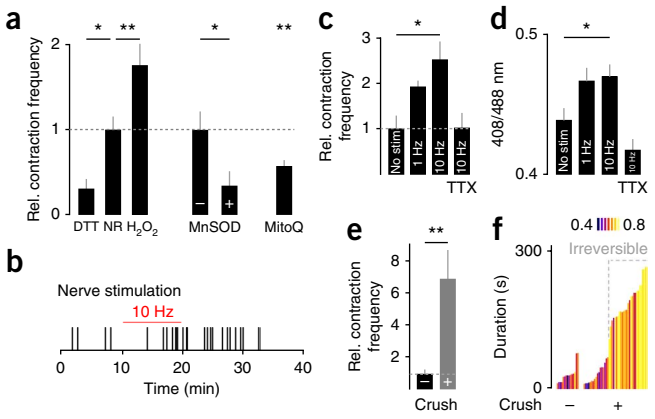

Figure 3 Mitochondrial contractions occur in response to physiological and pathological stressors. (**a**) Comparison of the relative frequency of contractions (Rel. contraction frequency) after addition of DTT, MitoQ and H_2O_2, and in MnSOD transgenic mice (n = 13–22 recordings from 3 mice per group. Analysis of variance (ANOVA) with Bonferroni *post hoc* testing for DTT, NR and H_2O_2 comparisons, $^*P < 0.05$ and $^{**}P < 0.01$. Two-tailed *t*-test for MitoQ versus NR, $^{**}P < 0.01$). The number of contractions is normalized to the number of contractions observed in normal Ringer's solution or in littermate controls (MnSOD, $^*P < 0.05$, two-tailed *t*-test). Dashed gray line indicates baseline levels. (**b**) Representative event plot illustrating the occurrence of contractions. Red bar shows the period of electrical stimulation at 10 Hz. The increased contraction frequency is sustained beyond the stimulation period. (**c**) Bar graphs showing the relative frequency of contractions before (no stim) and during stimulation (1 Hz and 10 Hz, n = 14–16 recordings from 5 mice per group; $^*P < 0.05$, Kruskal-Wallis test with Dunn *post hoc* analysis). Tetrodotoxin (TTX, 1 µM) was used to block action potential propagation (n = 12 recordings from 3 mice). Dashed gray line indicates baseline levels. (**d**) Redox state (ratio of 408-nm and 488-nm excitation) of mitochondria during stimulation experiments (n = 98–113 mitochondria from 3 mice per group, $^*P < 0.05$, ANOVA with Bonferroni *post hoc* testing). (**e**) Number of contractions before and after crush (n = 16 and 19 recordings from 6 and 5 mice, respectively, $^{**}P < 0.01$, Mann-Whitney *U*-test). (**f**) Duration of contractions before and after crush (n = 15 and 42 contractions from 5 mice per group, respectively). Each spike represents the duration of a single contraction (ordered by increasing duration). Contractions were considered irreversible if they lasted for at least 100 s and did not recover within the imaging period. Spikes are pseudocolored according to the redox state of the mitochondrion during the contraction. Graphs show mean ± s.e.m.

940 nm by tuning the Ti:Sapphire laser between these wavelengths, which allows for (slow) ratiometric measurements of the mitochondrial redox state over a broad range of exogenous H_2O_2 doses. We used *in vivo* laser axotomies to transect superficial spinal axons and induce acute axonal degeneration[16]. Two-photon ratiometric imaging revealed that mitochondrial oxidation occurred within minutes after transection and persisted for at least 4 h. We obtained similar results by mechanical spinal cord injury (**Supplementary Fig. 5**). *In vivo* analysis with single-organelle resolution further revealed that mitochondria at the lesion site showed high-level oxidation and irreversible shape changes, whereas at a distance of 300–400 µm from the lesion, mitochondria were less oxidized and some maintained normal shape. To visualize the initial spread of mitochondrial changes along individual transected axons, we devised a fast *in vivo* confocal microscopy approach based on line-sequential scanning of images with 405- and 488-nm laser light. This enabled us to concomitantly resolve mitochondrial shape and redox changes with submicron *xy* resolution at frame rates of around 0.2 Hz. We found that mitochondria close to the lesion site were oxidized within ~5 s after axotomy (**Fig. 4a,b** and **Supplementary Video 6**). Oxidation then spread along the axon with an initial speed of ~2.4 µm/s for a distance of at least 150 µm away from the transection site. Oxidation was accompanied by mitochondrial swelling and fragmentation, which progressed at a slower rate (~1.4 µm/s, **Fig. 4c**).

Next, we addressed the molecular mechanisms that might drive the spread of mitochondrial oxidation and damage. We first assessed whether oxidative stress is a cause or consequence of mitochondrial damage. Transgenic overexpression of MnSOD or application of

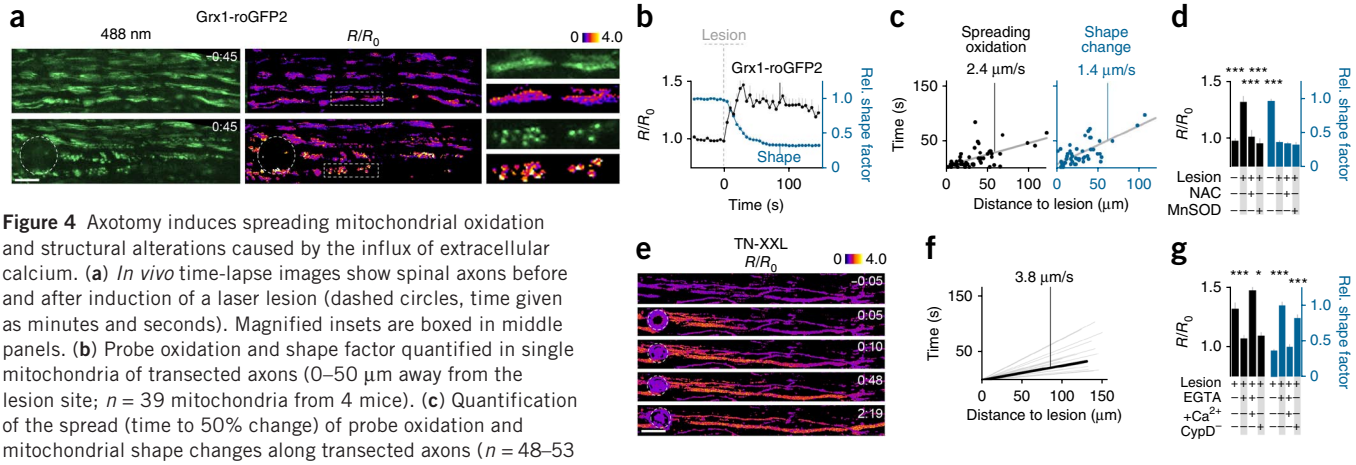

Figure 4 Axotomy induces spreading mitochondrial oxidation and structural alterations caused by the influx of extracellular calcium. (**a**) *In vivo* time-lapse images show spinal axons before and after induction of a laser lesion (dashed circles, time given as minutes and seconds). Magnified insets are boxed in middle panels. (**b**) Probe oxidation and shape factor quantified in single mitochondria of transected axons (0–50 µm away from the lesion site; n = 39 mitochondria from 4 mice). (**c**) Quantification of the spread (time to 50% change) of probe oxidation and mitochondrial shape changes along transected axons (n = 48–53 mitochondria from 4 mice). (**d**) Quantification of mitochondrial shape changes and oxidation in lesioned (Lesion +) spinal axons. NAC, treatment with 1 mM *N*-acetylcysteine; MnSOD, transgenic overexpression of MnSOD. All statistical tests were performed in comparison to Lesion + condition; all values are normalized to mean before injury (n = 15–40 mitochondria from 3 mice for each condition, $P < 0.001$, ANOVA with Bonferroni *post hoc* testing). (**e**) *In vivo* two-photon time-lapse recording of the calcium increase in spinal axons induced by laser lesion (dashed circles) in *Thy1*-TN-XXL mice (time in minutes and seconds before and after axotomy). (**f**) Speed of calcium spread along transected axons. The light gray lines represent the average speed for individual axons; their length indicates the distance of the most distal measurement point from the lesion (n = 16 axons from 3 mice). (**g**) Quantification of mitochondrial shape changes and oxidation after spinal cord injury. EGTA, depletion of extracellular calcium; +Ca, return to extracellular solution containing standard calcium levels; $CypD^-$, cyclophilin D-deficient mice. All statistical tests were performed in comparison to Lesion + condition and values normalized to mean before injury (n = 14–40 mitochondria from 3 mice for each condition, $^*P < 0.05$, $^{***}P < 0.001$, ANOVA with Bonferroni *post hoc* testing). Graphs show mean ± s.e.m. Scale bars, 10 µm in **a** and 25 µm in **e**.

N-acetylcysteine (1 mM) prevented mitochondrial oxidation but not structural damage (**Fig. 4d**), indicating that shape changes occur independently of redox changes. As structural damage is initiated at the transection site, we further investigated whether local calcium influx through the disrupted axonal membrane might trigger the damage cascade. To test this, we measured intra-axonal calcium levels in *Thy1*-TN-XXL mice, which express a fluorescence resonance energy transfer–based calcium sensor in neurons[17]. Laser transection led to a localized calcium influx at the transection site that spread along the axons at ~3.8 µm/s, ahead of the subsequent mitochondrial redox changes (**Fig. 4e**,**f** and **Supplementary Video 7**). Incubating the spinal cord with an EGTA-containing calcium-free solution revealed that the intra-axonal calcium rise depends on extracellular calcium and is necessary and sufficient for the induction of mitochondrial oxidation and damage (**Fig. 4g**). One possible explanation is that axotomy-induced calcium overload results in mitochondrial permeability transition[27]. Indeed, genetic suppression of permeability transition pore opening in cyclophilin D–deficient mice[27] resulted in delayed and blunted mitochondrial shape changes and oxidation (**Fig. 4g**).

DISCUSSION

In neurons, numerous signaling pathways intersect, often carrying parallel streams of information that are encoded by timing, spatial compartmentalization or amplitude modulation. Not surprisingly, dysregulation of such signaling can manifest as neuronal malfunction and hence neurological disease. One prime example of such complex signaling is provided by calcium, a central second messenger in neurons. *In vivo* imaging combined with genetically encoded calcium indicators has proven uniquely useful in untangling the intricate calcium signal streams that coexist in neurons[30]. ROS are emerging as similarly complex signal carriers, as increasingly more physiological and disease-related roles for these once simple-appearing oxidants are being discovered. The growing appreciation of the role that ROS have in cellular physiology can, to a considerable degree, be traced back to the recent improvements and innovative applications of genetically encoded redox indicators (GERIs). Starting with roGFPs[21,22], and later followed by HyPer[19], GERIs have revealed, for example, important roles of redox changes in initiating regeneration[31,32] and in determining the selective vulnerability of neuron subtypes in neurodegenerative disorders[33]. However, GERI-based imaging approaches for the living mammalian nervous system are so far not available, partly because the response kinetics, spectral properties and chemical specificity of first-generation GERIs were suboptimal for *in vivo* imaging. In particular, experiments using cpYFP-based redox probes are easily confounded by pH changes, especially when these probes are expressed in the mitochondrial matrix[20,23,34]. In contrast, ratiometric measurements with roGFPs are insensitive to pH changes in the physiological range[13,34]. Yet, the original roGFP2 has slow kinetics and is nonselectively modified by several oxidants[35]. Recently, roGFP2 has been engineered toward faster kinetics and higher specificity by coupling it to the glutathione redox pair using Grx1, resulting in the Grx1-roGFP2 sensor used here[13]. We developed imaging approaches using polychromator-based wide-field, two-photon and confocal microscopy that allow ratiometric imaging of transgenically expressed Grx1-roGFP2 *in vivo*. Moreover, we demonstrated how redox imaging can be integrated in a multiparametric optical approach that monitors key parameters of mitochondrial function and dysfunction.

One challenge in using GERIs *in vivo* is that most of the available sensors are excitation-ratiometric probes, which require switching excitation wavelengths quickly compared to the speed of movement artifacts, which are unavoidable in living mammals. We show that this challenge can be overcome, even in a demanding *in vivo* setting such as the injured spinal cord, by using adaptations of widely available imaging modalities, such as two-photon and excitation-ratiometric confocal microscopy. Such imaging can be transferred to any site in the nervous system that shows expression in our mice and that can be accessed by *in vivo* imaging, such as the cerebral cortex (**Supplementary Fig. 6**). This allows a comprehensive *in vivo* characterization of mitochondrial dynamics, redox signaling and bioenergetics at the single-organelle level in a wide variety of physiological and pathological settings.

Here we demonstrate the analytical power of GERI-based imaging approaches by mechanistically deconstructing and differentiating two forms of mitochondrial redox signals. We achieved this by multiparametric *in vivo* imaging to assess mitochondrial shape, redox state, pH, calcium levels and membrane potential. For example, our results suggest that mitochondrial contractions could be explained by the following sequence of events: initially, endogenous or exogenous stressors induce a mild oxidation of mitochondria that primes them for the contraction process. Then, contraction is initiated by rapid depolarization that is probably mediated by spontaneous ion flux and charge equilibration across the inner mitochondrial membrane. These ion fluxes could be carried by potassium or sodium ions, but, according to our results, are less likely to involve calcium ions or protons (although smaller fluxes that are below the detection threshold of the corresponding biosensors could also contribute). Next, the reduced mitochondrial membrane potential leads to the acceleration of electron transport and, as a result, to increased pumping of protons out of the matrix, which explains the alkaline spike observed with the mitochondrial pH sensor. Increased activity of the electron transport chain and subsequent ROS generation could induce activation of uncoupling proteins that mediate sustained matrix acidification and potential decrease. As the frequency of such spontaneous contractions was increased by physiological (electrical activity) and pathological (nerve crush and neurodegeneration) stress, and transient uncoupling has been shown to protect mitochondria from lasting damage[33], we suggest that contractions act as a 'safety fuse' that allow mitochondria to overcome acute challenges. As several forms of mitochondrial paroxysms, such as pulses[36], pH flashes[37] and putative superoxide bursts[38], have been discovered and linked to disease[26], the ability to mechanistically disambiguate these phenomena may be a major application for our technique.

These transient and possibly protective changes in mitochondrial shape and redox state contrast with the more permanent mitochondrial damage observed when axons are severely injured. We studied such permanent organelle damage after axotomy, where we found a central role for calcium in mitochondrial damage. Calcium uptake and subsequent mitochondrial permeability transition resulted in mitochondrial oxidation and fragmentation. In contrast to contractions, oxidation did not trigger changes in mitochondrial shape. Thus, our approach revealed two mechanistically distinct forms of mitochondrial dynamics: permanent, calcium-dependent alterations and more transient, redox-driven alterations. Such insights are crucial for deciphering the increasingly appreciated role of mitochondria in neuronal health and disease[6,9].

METHODS

Methods and any associated references are available in the online version of the paper.

Note: Any Supplementary Information and Source Data files are available in the online version of the paper.

ACKNOWLEDGMENTS

We thank G. Heitmann, M. Adrian and K. Wullimann for technical assistance, D. Matzek, M. Budak, N. Budak and L. Marinković for animal husbandry and M. Krumbholz for help with statistical analysis. We thank M. Murphy (University of Cambridge) for the gift of MitoQ. We thank R. Campbell (University of Alberta) for the R-GECO1 plasmid, L. Looger (Howard Hughes Medical Institute Janelia Farm Research Campus) for GCaMP3 and N. Demaurex (University of Geneva Medical School) for mito-SypHer. Work in M.K.'s laboratory is financed through grants from the Deutsche Forschungsgemeinschaft (DFG; Sonderforschungsbereich 870 and Transregio 128), the German Federal Ministry of Research and Education (BMBF, Competence Network Multiple Sclerosis), the European Research Council (ERC) under the European Union's Seventh Framework Program (FP/2007-2013; ERC grant agreement no. 310932), the Hertie Foundation and the 'Verein Therapieforschung für MS-Kranke e.V.' T.M. is supported by the Institute of Advanced Studies (Technische Universität München), the Alexander von Humboldt Foundation, the Center for Integrated Protein Science (Munich, EXC 114), the DFG (SFB 596) and the DZNE (Munich). T.M.'s work on this project was further supported by the BMBF as part of ERA-Net '2-photon imaging'. F.M.B. is supported by the DFG (SFB 870) and an independent group leader award of the BMBF. F.M.B., M.K. and T.M. are supported by SyNergy (EXC 1010), and T.P.D., M.K. and T.M. are supported by the DFG Priority Program 1710. Work in D.K.S.C.'s laboratory is supported by grants from the US National Institutes of Health Ca 049797 and the Edward P. Evans Foundation. T.P.D. is supported by the DFG (SFB 938, SFB 1036) and the BMBF ('LungSys'). M.O.B. is recipient of a doctoral fellowship from the Gertrud Reemtsma Foundation (Max Planck Society) and is supported by the German National Academic Foundation. P.R.W. is supported by a postdoctoral fellowship from the Wings of Life Foundation and received previous support from the Human Frontier Science Program. M.O.B. and P.M. were supported by the Graduate School of Technische Universität München.

AUTHOR CONTRIBUTIONS

T.M., M.K., T.P.D. and M.O.B. conceived of the experiments. M.O.B., F.M.J.P., P.R.W., M.K. and T.M. performed imaging experiments and image analysis. F.M.B., L.G., T.P.D., O.G., M.S.B., B.P., R.N., D.K.S.C., F.M.J.P. and M.O.B. generated and characterized transgenic mouse lines. P.M.B. performed virus injections. A.S. generated AAV vectors. P.M. and F.M.J.P. conducted experiments in the ALS model. M.K., T.M., M.S. and M.O.B. interpreted the experiments and wrote the paper.

COMPETING FINANCIAL INTERESTS

The authors declare no competing financial interests.

1. D'Autréaux, B. & Toledano, M.B. ROS as signalling molecules: mechanisms that generate specificity in ROS homeostasis. *Nat. Rev. Mol. Cell Biol.* **8**, 813–824 (2007).
2. Albrecht, S.C., Barata, A.G., Großhans, J., Teleman, A.A. & Dick, T.P. *In vivo* mapping of hydrogen peroxide and oxidized glutathione reveals chemical and regional specificity of redox homeostasis. *Cell Metab.* **14**, 819–829 (2011).
3. Niethammer, P., Grabher, C., Look, A.T. & Mitchison, T.J. A tissue-scale gradient of hydrogen peroxide mediates rapid wound detection in zebrafish. *Nature* **459**, 996–999 (2009).
4. Dickinson, B.C., Peltier, J., Stone, D., Schaffer, D.V. & Chang, C.J. Nox2 redox signaling maintains essential cell populations in the brain. *Nat. Chem. Biol.* **7**, 106–112 (2011).
5. Guarente, L. Mitochondria—A nexus for aging, calorie restriction, and sirtuins? *Cell* **132**, 171–176 (2008).
6. Lin, M.T. & Beal, M.F. Mitochondrial dysfunction and oxidative stress in neurodegenerative diseases. *Nature* **443**, 787–795 (2006).
7. Murphy, M.P. How mitochondria produce reactive oxygen species. *Biochem. J.* **417**, 1–13 (2009).
8. Zorov, D.B., Filburn, C.R., Klotz, L.O., Zweier, J.L. & Sollott, S.J. Reactive oxygen species (ROS)-induced ROS release: a new phenomenon accompanying induction of the mitochondrial permeability transition in cardiac myocytes. *J. Exp. Med.* **192**, 1001–1014 (2000).
9. Nunnari, J. & Suomalainen, A. Mitochondria: in sickness and in health. *Cell* **148**, 1145–1159 (2012).
10. Mahad, D.J. *et al.* Mitochondrial changes within axons in multiple sclerosis. *Brain* **132**, 1161–1174 (2009).
11. Nikić, I. *et al.* A reversible form of axon damage in experimental autoimmune encephalomyelitis and multiple sclerosis. *Nat. Med.* **17**, 495–499 (2011).
12. Sullivan, P.G., Krishnamurthy, S., Patel, S.P., Pandya, J.D. & Rabchevsky, A.G. Temporal characterization of mitochondrial bioenergetics after spinal cord injury. *J. Neurotrauma* **24**, 991–999 (2007).
13. Gutscher, M. *et al.* Real-time imaging of the intracellular glutathione redox potential. *Nat. Methods* **5**, 553–559 (2008).
14. Misgeld, T., Kerschensteiner, M., Bareyre, F.M., Burgess, R.W. & Lichtman, J.W. Imaging axonal transport of mitochondria *in vivo*. *Nat. Methods* **4**, 559–561 (2007).
15. Gurney, M.E. *et al.* Motor neuron degeneration in mice that express a human Cu,Zn superoxide dismutase mutation. *Science* **264**, 1772–1775 (1994).
16. Kerschensteiner, M., Schwab, M.E., Lichtman, J.W. & Misgeld, T. *In vivo* imaging of axonal degeneration and regeneration in the injured spinal cord. *Nat. Med.* **11**, 572–577 (2005).
17. Mank, M. *et al.* A genetically encoded calcium indicator for chronic *in vivo* two-photon imaging. *Nat. Methods* **5**, 805–811 (2008).
18. Wardman, P. Fluorescent and luminescent probes for measurement of oxidative and nitrosative species in cells and tissues: progress, pitfalls, and prospects. *Free Radic. Biol. Med.* **43**, 995–1022 (2007).
19. Belousov, V.V. *et al.* Genetically encoded fluorescent indicator for intracellular hydrogen peroxide. *Nat. Methods* **3**, 281–286 (2006).
20. Schwarzländer, M., Logan, D.C., Fricker, M.D. & Sweetlove, L.J. The circularly permuted yellow fluorescent protein cpYFP that has been used as a superoxide probe is highly responsive to pH but not superoxide in mitochondria: implications for the existence of superoxide 'flashes'. *Biochem. J.* **437**, 381–387 (2011).
21. Hansen, J.M., Go, Y.-M. & Jones, D.P. Nuclear and mitochondrial compartmentation of oxidative stress and redox signaling. *Annu. Rev. Pharmacol. Toxicol.* **46**, 215–234 (2006).
22. Dooley, C.T. *et al.* Imaging dynamic redox changes in mammalian cells with green fluorescent protein indicators. *J. Biol. Chem.* **279**, 22284–22293 (2004).
23. Schwarzländer, M. *et al.* Mitochondrial 'flashes': a radical concept repHined. *Trends Cell Biol.* **22**, 503–508 (2012).
24. Poburko, D., Santo-Domingo, J. & Demaurex, N. Dynamic regulation of the mitochondrial proton gradient during cytosolic calcium elevations. *J. Biol. Chem.* **286**, 11672–11684 (2011).
25. Zhao, Y. *et al.* An expanded palette of genetically encoded Ca^{2+} indicators. *Science* **333**, 1888–1891 (2011).
26. Wang, J.-Q. *et al.* Dysregulation of mitochondrial calcium signaling and superoxide flashes cause mitochondrial genomic DNA damage in Huntington disease. *J. Biol. Chem.* **288**, 3070–3084 (2013).
27. Schinzel, A.C. *et al.* Cyclophilin D is a component of mitochondrial permeability transition and mediates neuronal cell death after focal cerebral ischemia. *Proc. Natl. Acad. Sci. USA* **102**, 12005–12010 (2005).
28. Keller, J.N. *et al.* Mitochondrial manganese superoxide dismutase prevents neural apoptosis and reduces ischemic brain injury: suppression of peroxynitrite production, lipid peroxidation, and mitochondrial dysfunction. *J. Neurosci.* **18**, 687–697 (1998).
29. Yanik, M.F. *et al.* Neurosurgery: functional regeneration after laser axotomy. *Nature* **432**, 822 (2004).
30. Grienberger, C. & Konnerth, A. Imaging calcium in neurons. *Neuron* **73**, 862–885 (2012).
31. Love, N.R. *et al.* Amputation-induced reactive oxygen species are required for successful *Xenopus* tadpole tail regeneration. *Nat. Cell Biol.* **15**, 222–228 (2013).
32. Rieger, S. & Sagasti, A. Hydrogen peroxide promotes injury-induced peripheral sensory axon regeneration in the zebrafish skin. *PLoS Biol.* **9**, e1000621 (2011).
33. Guzman, J.N. *et al.* Oxidant stress evoked by pacemaking in dopaminergic neurons is attenuated by DJ-1. *Nature* **468**, 696–700 (2010).
34. Roma, L.P. *et al.* Dynamic measurements of mitochondrial hydrogen peroxide concentration and glutathione redox state in rat pancreatic β-cells using ratiometric fluorescent proteins: confounding effects of pH with HyPer but not roGFP1. *Biochem. J.* **441**, 971–978 (2012).
35. Meyer, A.J. & Dick, T.P. Fluorescent protein-based redox probes. *Antioxid. Redox Signal.* **13**, 621–650 (2010).
36. Schwarzländer, M. *et al.* Pulsing of membrane potential in individual mitochondria: a stress-induced mechanism to regulate respiratory bioenergetics in *Arabidopsis*. *Plant Cell* **24**, 1188–1201 (2012).
37. Santo-Domingo, J., Giacomello, M., Poburko, D., Scorrano, L. & Demaurex, N. OPA1 promotes pH flashes that spread between contiguous mitochondria without matrix protein exchange. *EMBO J.* **32**, 1927–1940 (2013).
38. Wang, W. *et al.* Superoxide flashes in single mitochondria. *Cell* **134**, 279–290 (2008).

ONLINE METHODS

Animals. To selectively express redox sensors in neuronal mitochondria, we used a modified version of the *Thy1* promoter to drive the expression of mito-Grx1-roGFP2 (ref. 13), in which the mitochondrial targeting sequence from ATP synthase protein 9 (*Neurospora crassa*) is fused to Grx1-roGFP2. Constructs were cloned by standard procedures as previously described[39], and founders were generated by pronuclear injections. We screened 11 founder lines for expression of the fluorescent sensor proteins, of which four (lines 676, 690, 920 and 924) were further characterized. *Thy1*-TN-XXL mice, which express the troponin C–based calcium sensor TN-XXL[17] in neurons, were used to detect changes in intra-axonal calcium levels. MnSOD-overexpressing mice[28], cyclophilin D–deficient mice[27] and SOD^{G93A} mice (Tg(SOD1*G93A)1Gur/J; The Jackson Laboratory)[15] were crossed to *Thy1*-mito-Grx1-roGFP2 animals. *Thy1*-mito-TagRFP-t mice, which express a red fluorescent protein[40] in neuronal mitochondria, were generated as described previously for *Thy1*-mito-CFP mice[14]. Both mouse strains with labeled neuronal mitochondria were used for morphological and ratiometric imaging and expressed the transgene in a similar pattern (**Supplementary Fig. 7** and **Supplementary Table 1**). We used adult male and female animals (older than 6 weeks and up to ~8 months of age) for our experiments. All animal work conformed to institutional guidelines and was approved by the Animal Study Committee of the Regierung von Oberbayern.

Preparation, staining and analysis of fixed tissue. For tissue analysis, mice were transcardially perfused with 4% (wt/vol) paraformaldehyde (PFA) diluted in 1× PBS and postfixed for 24 h in 4% PFA in PBS. Following dissection, the tissue of interest (brain, spinal cord and eye) was either prepared for cryosectioning by incubation in 30% sucrose (Sigma) or vibratome sectioned. Sections (30–50 µm thick) were stained with NeuroTrace 640/660 (Molecular Probes, diluted 1:500) to label cell bodies and nuclei or with Alexa Fluor 594–conjugated α-bungarotoxin (Invitrogen, diluted 1:50 in PBS) to visualize acetylcholine receptors at the neuromuscular junction (NMJ). Tissue sections were mounted in Vectashield (Vector Laboratories), and image stacks were recorded using an FV1000 confocal microscope (Olympus) equipped with ×20/0.8 N.A. and ×60/1.42 N.A. oil-immersion objectives.

Imaging mitochondrial redox signals in triangularis sterni explants. Explants of the triangularis sterni muscle were prepared as previously described[14]. Briefly, mice were euthanized with isoflurane, and the rib cage (with the attached triangularis sterni muscle and its innervating intercostal nerves) of each mouse was isolated by paravertebral cuts, pinned in a Sylgard-coated dish using insect pins and maintained on a heated stage (32–35 °C) in normal Ringer's solution (125 mM NaCl, 2.5 mM KCl, 1.25 mM NaH_2PO_4, 26 mM $NaHCO_3$, 2 mM $CaCl_2$, 1 mM $MgCl_2$ and 20 mM glucose), bubbled with 95% O_2 5% CO_2. Recordings were performed in intercostal axons or at NMJs.

To record the mitochondrial redox state in motor axons and NMJs, we used a BX51 wide-field microscope (Olympus) equipped with ×20/0.5 NA and ×100/1.0 NA dipping-cone water-immersion objectives, a cooled charged-coupled device camera and either a filter wheel with shutter (controlled by µManager software[41]) or a PolyV polychromator system (Till Photonics, controlled by TillVision software; dichroic filter: D/F 500 DCXR; emission filter: ET 525/36). Images were acquired at rates of 0.5–1 Hz with exposure times of 150 ms for 408 nm excitation and 30 ms for 488 nm excitation.

Using this setup, we performed a series of experiments: For dose-response studies of the sensor proteins, we incubated triangularis sterni explants with DTT (Sigma or VWR; concentration of 500 µM diluted in Ringer's solution), followed by exogenous H_2O_2 (Sigma; concentrations of 6.25, 12.5, 25, 50, 100, 200, 400, 800 and 1,000 µM H_2O_2 diluted in Ringer's solution) for 3–5 min. For each condition, we acquired single-frame images of NMJs (3–10 NMJs per concentration per animal) after excitation with 408 and 488 nm. To measure the physiological redox state of mitochondria, we recorded time-lapse movies in intercostal nerves for 5 to 10 min at 0.5–1 Hz. During these time-lapse recordings, we observed spontaneous mitochondrial contractions. We quantified the frequency of contractions in relation to the absolute number of imaged mitochondria or in relation to the axonal area that was imaged.

To investigate mitochondrial changes after nerve crush, triangularis sterni explants were prepared as described above. Moderate pressure was manually applied under visual guidance to the intercostal nerve using fine metal forceps for 5–10 s. Imaging at 1 Hz was started immediately after the crush adjacent to the lesion site.

To explore mitochondrial redox changes during chronic neurodegeneration, we used a well-established ALS model based on the overexpression of a mutated form of the human superoxide dismutase-1 protein (SOD^{G93A}). Triangularis sterni explants were prepared as described above from double heterozygous SOD^{G93A} × *Thy1*-mito-Grx1-roGFP2 mice or SOD^{G93A} × *Thy1*-mito-CFP-C mice at postnatal days 10, 20, 60, 90, 120 and 135. SOD^{G93A}-negative littermates served as controls. The redox state of single mitochondria was assessed by wide-field fluorescence microscopy as described above.

The following pharmacological agents were used: cyclosporine A (20 µM; Sigma), genipin (100 µM; Sigma), MitoQ (1 µM), rotenone (0.1–100 nM; Sigma) and Ru360 (100 µM; Santa Cruz Biotechnology).

Controls for possible effects of phototoxicity and excision on redox dynamics. We performed several sets of experiments to control for the influence of phototoxicity and surgical procedures on the described behavior of mitochondria (data not shown). First, mitochondria that showed the characteristic pearl-on-string morphology of contracting mitochondria were found in nerve tissue that was perfusion-fixed before isolation and imaging. Second, as high levels of light can induce additional contractions (as light can induce ROS), we chose our imaging conditions to conform to low light levels that had a minimal impact on baseline contraction frequencies (data not shown). Indeed, even at the lowest exposure times tested (4 ms for 488 nm and 19 ms for 408 nm), contractions could be discerned with similar frequencies to those seen under our standard conditions. Third, neither the oxidation of mitochondria nor the frequency of contractions increased over the course of imaging, suggesting that there is no cumulative toxicity. Fourth, contractions could be observed with many different fluorophores in several anatomical sites using different excitation wavelengths and different types of microscopy. Together, these methods cover orders of magnitude of illumination and should induce very variable levels of phototoxicity.

Imaging the mitochondrial potential, pH and calcium. To analyze the mitochondrial membrane potential, we first surgically exposed the third and fourth intercostal nerves of anesthetized *Thy1*-mito-Grx1-roGFP2 or *Thy1*-mito-CFP-C mice in the axillary line and implanted a gel foam pad soaked with 2.5 µl of TMRM (Invitrogen; concentration 25 mM in DMSO) onto the intercostal nerve. The pectoralis muscle was sutured in place to secure the gel foam. Mice were allowed to recover in a preheated chamber. Triangularis sterni explants were prepared 1–7 d after gel foam implantation. The mitochondrial membrane potential of single mitochondria in intercostal nerve axons was assessed in parallel to the glutathione redox potential by triple-wavelength imaging with a triple-dichroic filter set (DAPI/FITC/TRITC set) using excitation at 408, 488 and 550 nm. For co-imaging of TMRM and CFP, a triple-dichroic filter set (CFP/YFP/DsRed set) using excitation at 440 and 570 nm was used. Movies were recorded for 5–10 min at 0.5 Hz. For assessing additional metabolic parameters of mitochondria in triangularis sterni explants, we injected recombinant adeno-associated virus particles (rAAV-1/2, virions containing a 1:1 ratio of AAV1 and AAV2 capsid proteins) into the cervical spinal cord, targeting motor neurons in the ventral horn that give rise to intercostal axons that project to the triangularis sterni muscle. The injection level was C7–T1 lateral to the midline at a depth of 0.9 mm below the dural surface, and each virus was diluted 1:2 in sterile PBS. rAAV-mito-GCaMP3 (ref. 42) (mitochondrial calcium, titer: 2.68×10^{11} particles/ml; GCaMP3 Addgene plasmid 22692), rAAV-mito-R-GECO1 (ref. 25) (mitochondrial calcium, titer: 1.32×10^{11} particles/ml; R-GECO1 Addgene plasmid 32444) and rAAV-mito-SypHer[24] (matrix pH, titer 1.01×10^{11} particles/ml) were cloned and produced in AAV-293 (Invitrogen) by standard methods[43,44]. Triangularis sterni explants were prepared 2–4 weeks after virus injection. rAAV-mito-GCaMP3 was injected into *Thy1*-mito-TagRFP-t and ratiometrically imaged with standard GFP and rhodamine filter sets. rAAV-mito-R-GECO1 and rAAV-mito-SypHer were injected into wild-type (C57BL/6) mice and imaged

with a standard rhodamine filter set or as described for Grx1-roGFP2, respectively. Laser lesions were induced in triangularis sterni explants as described below and imaged with the appropriate confocal laser lines, dichroic mirrors and filter sets for each sensor.

***In vivo* two-photon imaging of mitochondrial redox changes in the spinal cord.** To image mitochondrial redox changes in spinal axons, we adapted the spinal cord imaging technique we previously described[45]. Briefly, the animal was anesthetized by intraperitonal injection of ketamine (87 mg per kg body weight (mg/kg)) and xylazine (13 mg/kg), and the spinal cord was surgically exposed by a lumbar laminectomy (vertebrae L1–L3). Anesthesia was maintained by re-injection of one-half the initial dose of anesthetic every 90 min. For two-photon experiments, the dura mater was kept intact. The surgical opening was surrounded with 2% agarose in PBS, and the resulting reservoir was superfused with mouse artificial cerebrospinal fluid (maCSF). For two-photon imaging, we used an FV1000 MPE microscope (Olympus) equipped with a femtosecond-pulsed Ti:Sapphire laser (Mai Tai HP, Newport/Spectra-Physics) and a high numerical aperture water-immersion objective (×25/1.05 N.A.). Small *z* stacks (3 images with a *z* distance of 0.8–1 µm) of the superficial dorsal spinal cord were acquired.

To determine the two-photon emission spectra of the Grx1-roGFP2 sensor *in vivo*, we first reduced the sensor with DTT (200 mM, diluted in maCSF), tuned the two-photon laser excitation in 10-nm steps from 750 to 980 nm and recorded images for each step. Next, we oxidized the sensor with H_2O_2 (50 mM, diluted in maCSF) and repeated the procedure. By comparing the spectra of the oxidized and reduced sensor, we determined the optimal wavelength combination for ratiometric measurements (800/940 nm). For *in vivo* dose-response studies of the Grx1-roGFP2 sensor in neuronal mitochondria, we first applied 200 mM DTT diluted in maCSF to the exposed spinal cord to reduce the sensor and added increasing doses of H_2O_2 (0.5, 1, 2.5, 5, 10, 50 and 100 mM H_2O_2 diluted in maCSF; these high levels of H_2O_2 are necessary to penetrate the dura and do not reflect the actual concentrations in the spinal cord; see calibration in explants). After 5 min of incubation time, image stacks were acquired for each step using excitation wavelengths at 800 and 940 nm as described above (**Supplementary Fig. 4**).

To record mitochondrial redox changes after axon injury, we performed laser axotomies[29] in the spinal cord of living mice. For this purpose, the two-photon laser was tuned to 760–800 nm, and the power was increased to 100% (~2.9 W laser output) and focused on a small circle (diameter ~25 µm) for 90 s. After laser exposure, a local increase in fluorescence indicated the site of axon transection. To follow mitochondrial changes over time, we acquired image stacks every 5 min during the first hour and every 10 min for the rest of the experiment. For inducing a mechanical spinal cord injury, a hypodermic needle was used as described previously[16].

***In vivo* confocal imaging of mitochondrial redox changes.** To image alterations of mitochondrial shape and redox state with higher temporal resolution in the spinal cord or to perform laser axotomies in the triangularis sterni explant, we used an FV1000 MPE microscope (Olympus) equipped with a femtosecond-pulsed Ti:Sapphire laser (Mai Tai HP, Newport/Spectra-Physics), as well as 405- and 488-nm laser lines for single-photon excitation and ×40/0.8 NA or ×25/1.1 NA water-immersion objectives (Nikon). For imaging spinal axons, we exposed the spinal cord of *Thy1*-mito-Grx1-roGFP2 mice as described above. The dura was removed, and axons in the superficial dorsal spinal cord were selected. These axons were then laser transected using the protocol described above, but lower laser power (1.9 W laser output) and shorter laser exposure (5–10 s) were used to minimize the lesion (diameter ~25 µm). To rapidly alternate 405- and 488-nm excitation, we sequentially scanned lines with 405- and 488-nm laser excitation (line scan duration: ~4.5 ms) and collected the emission light (band-pass filter, 492–592 nm) in separate channels using a 50/50 beam splitter. For additional imaging of red-shifted sensors, a 559-nm laser line was used in addition. Small *z* stacks (4 or 5 images with a *z* distance of 1 µm) were acquired at a frame rate of 0.1–0.2 Hz. For evaluation (detailed below), acquisition times were binned to 0.2 Hz, as frame rates differed slightly between experiments. Laser axotomies in the triangularis sterni explant followed the same protocol. For pharmacological interventions, *N*-acetylcysteine (NAC, 1 mM; Sigma) was diluted in maCSF. To determine the role of extracellular calcium, 5 mM EGTA was added to maCSF, in which Ca^{2+} was replaced by Mg^{2+}. As aversive effects of anesthesia on mitochondria have been reported in the literature[46,47], additional types of anesthesia were tested to confirm that the observed mitochondrial alterations following axotomy were not affected. A triple-injection anesthesia consisting of 0.05 mg/kg fentanyl, 5 mg/kg midazolam and 0.5 mg/kg medetomidin and an inhalation anesthesia protocol using 1–2% isoflurane administered via a tracheal tube served as controls. These showed a similar pattern of mitochondrial oxidation and fragmentation following axotomy as observed in experiments using ketamine/xylazine anesthesia (data not shown).

For cortical *in vivo* imaging, the skull of *Thy1*-mito-Grx1-roGFP2 mice was thinned as described previously[48]. Superficial regions of the cortex were imaged where single mitochondria could be discerned. A line scan of the two-photon laser was used to induce a laser lesion in the cortex, and mitochondrial redox and shape changes were imaged by confocal microscopy as described above for the spinal cord (imaging speed was ~0.2 Hz).

***In vivo* two-photon imaging of axonal calcium levels in the spinal cord.** For determining intra-axonal calcium changes after axotomy, we used *Thy1*-TN-XXL mice[17]. Axotomies were induced as described above, and imaging was performed on an FV1000 MPE microscope (Olympus) equipped with a femtosecond-pulsed Ti:Sapphire laser (Mai Tai HP, Newport/Spectra-Physics) and a high numerical aperture water-immersion objective (×0.25/1.05 N.A.). The sensor was excited at 840 nm and imaged at a frame rate of ~0.2 Hz. Signals were recorded in two parallel channels (dichroic mirror: 505 nm; band-pass filters 460–500 nm for CFP and 520–560 nm for YFP).

Image processing and analysis. Images were analyzed using the open-source software ImageJ/Fiji (http://fiji.sc). Single mitochondria or clusters of mitochondria and background regions were selected as regions of interest (ROI). Mean intensity values were measured in the 408-nm (or 405-nm and 800-nm in confocal or two-photon imaging, respectively) and 488-nm (940-nm) channel, and the background was subtracted. No background subtraction was performed when confocal *in vivo* imaging was performed, as this caused an artificial decrease of the baseline ratio owing to differential photobleaching. The background-corrected values for the two channels were divided (excitation at 408/488, 405/488 and 800/940 nm) to obtain a measure of the redox state of the sensor. This ratio was normalized to the mean ratio measured after reduction with DTT (R/R_{DTT}) in cases where DTT was used in the same experiment. Otherwise, the experimental results are shown either as R/R_0, with R_0 being the ratio at the time before the mitochondrial contraction or the axotomy, or normalized to a suitable control population (for example, R/R_{Rest} for analysis of mitochondrial movement, $R/R_{Control}$ for ALS mice). Measurements for mitochondrial potential (excitation at 570/440 nm if co-imaged with mito-CFP or 550 nm for single-wavelength measurements), pH (488/408 nm) and calcium (GCaMP-3 co-imaged with mito-TagRFP-t 488/550 nm; R-GECO1 550 nm) were performed in a similar way using the appropriate channels as indicated.

Mitochondrial shape is expressed as a 'shape factor' (length/width of the mitochondrion). The speed of spreading oxidation, mitochondrial calcium or shape changes after axotomy was defined as the distance of a mitochondrion from the lesion over the time it took to reach 50% of the maximal stable rise in sensor signal or to reach 50% of its maximal shape change. The time period used for determining the stable plateau was judged individually for each recording. The speed was derived by linear regression analysis.

For quadrant representation of single mitochondria, the quadrant border delineating increased probe oxidation was defined as two times the s.d. above the mean of the population with normal R/R_{DTT}. The quadrant border delineating altered mitochondrial shape was defined as two times the s.d. above the mean of the oxidized mitochondria (at postnatal day 135 in SOD^{G93A} mice or in the lesion area after laser axotomy).

For the generation of pseudocolor images, the 488-nm (940-nm) channel was manually 'thresholded' and 'binarized' to serve as a segmentation mask. This mask was used to segment both channels. The resulting images were divided (408/488 nm, 405/488 nm and 800/940 nm) and 'normalized' by the

doi:10.1038/nm.3520

DTT measurements (R/R_{DTT}) or the ratio before the event (contraction or lesion induction) (R/R_0). The spectral pseudocolor look-up table 'fire' (ImageJ/Fiji) was used to display images. These images were only used for representation, and aberrant noise pixels in the background were removed.

For quantifying calcium levels, ROIs were placed along the transected axon and on nonlesioned axons (outside) serving as controls. Both channels were background subtracted, and the YFP/CFP ratio was determined before and after the lesion (R/R_0). Pseudocolor representations were obtained as described above. To calculate the speed of intra-axonal calcium spread, the time to reach 50% of the maximal signal was used at several points along one axon. Speeds were calculated for each of these measurements to obtain the average speed for an individual axon. To analyze the spread of calcium and oxidation in comparable axon populations, we first determined the distribution of axon diameters in *Thy1*-mito-Grx1-roGFP2 mice crossed to other transgenic mice, which express a spectrally distinct cytoplasmic fluorescent protein under control of the *Thy1* promoter[49] and then included only axons within a similar population (mean ± 2 s.d. of the population measured in this cross) in the analysis of *Thy1*-TN-XXL mice.

For representation of multicolor micrographs, different channels of confocal image series were combined in pseudocolor using the 'screen' function in Photoshop software. To stitch multiple images into larger montages, masking was used to obscure borders between individual images. Gamma was adjusted nonlinearly to show low-intensity objects (except when quantitative results are represented), and a 'despeckle' filter was used in some panels to suppress detector noise. For stitched figures, combined objects were isolated with the 'magic wand' function in Photoshop and placed on a black background to remove distracting interference background patterns.

Statistical analyses. Statistical analysis was performed using Excel (Microsoft) and PRISM (GraphPad). Unless stated otherwise, we used two-tailed *t*-tests to compare two groups and one-way ANOVA with Bonferroni *post hoc* testing in cases of multiple comparisons. To assess differences in time-lapse recordings, we averaged each trace over a defined time period and compared the means using two-tailed *t*-tests. *P* values < 0.05 were considered to be significant and indicated by '*'; *P* values < 0.01 were indicated by '**' and < 0.001 by '***'. Graphs show mean ± s.e.m. Trend lines in **Figure 1e** and **Supplementary Fig. 4d** were calculated with PRISM, assuming a dose-response saturation kinetic. No statistical method was used to predetermine sample size. The investigators were not blinded to allocation during experiments and outcome assessment. The experiments were not randomized.

39. Marinkovic, P., Godinho, L. & Misgeld, T. in *Imaging in Neuroscience: a Laboratory Manual* (eds. Yuste, R. & Konnerth A.) Ch. 22 (Cold Spring Harbor Laboratory Press, 2011).
40. Shaner, N.C. *et al.* Improving the photostability of bright monomeric orange and red fluorescent proteins. *Nat. Methods* **5**, 545–551 (2008).
41. Edelstein, A., Amodaj, N., Hoover, K., Vale, R. & Stuurman, N. Computer control of microscopes using μManager. *Curr. Protoc. Mol. Biol.* **92**, 14.20 (2010).
42. Tian, L. *et al.* Imaging neural activity in worms, flies and mice with improved GCaMP calcium indicators. *Nat. Methods* **6**, 875–881 (2009).
43. Klugmann, M. *et al.* AAV-mediated hippocampal expression of short and long Homer 1 proteins differentially affect cognition and seizure activity in adult rats. *Mol. Cell. Neurosci.* **28**, 347–360 (2005).
44. Bareyre, F.M. *et al. In vivo* imaging reveals a phase-specific role of STAT3 during central and peripheral nervous system axon regeneration. *Proc. Natl. Acad. Sci. USA* **108**, 6282–6287 (2011).
45. Romanelli, E. *et al.* Cellular, subcellular and functional *in vivo* labeling of the spinal cord using vital dyes. *Nat. Protoc.* **8**, 481–490 (2013).
46. Zhang, Y. *et al.* Anesthetics isoflurane and desflurane differently affect mitochondrial function, learning, and memory. *Ann. Neurol.* **71**, 687–698 (2012).
47. Boscolo, A. *et al.* Early exposure to general anaesthesia disturbs mitochondrial fission and fusion in the developing rat brain. *Anesthesiology* **118**, 1086–1097 (2013).
48. Yang, G., Pan, F., Parkhurst, C.N., Grutzendler, J. & Gan, W.B. Thinned-skull cranial window technique for long-term imaging of the cortex in live mice. *Nat. Protoc.* **5**, 201–208 (2010).
49. Feng, G. *et al.* Imaging neuronal subsets in transgenic mice expressing multiple spectral variants of GFP. *Neuron* **28**, 41–51 (2000).